1　**Air-borne in-situ measurements of aerosol size distributions and**
2　**BC across the IGP during SWAAMI**

3　Mukunda Madhab Gogoi[1], Venugopalan Nair Jayachandran[1], Aditya Vaishya[2], Surendran Nair
4　Suresh Babu[1], Sreedharan Krishnakumari Satheesh[3,4] and Krishnaswamy Krishna Moorthy[3]

5　[1]Space Physics Laboratory, Vikram Sarabhai Space Centre, Thiruvananthapuram – 695022, India
6　[2]School of Arts and Sciences, Ahmedabad University, Ahmedabad – 380009, India
7　[3]Centre for Atmospheric and Oceanic Sciences, Indian Institute of Science, Bengaluru – 560012, India
8　[4]Divecha Centre for Climate Change, Indian Institute of Science, Bengaluru – 560012, India

9

10　**Abstract**

11　During the South-West Asian Aerosol Monsoon Interaction (SWAAMI) experiment, collocated air-
12　borne measurements of aerosol number-size distributions in the size (diameter) regime 0.5 to 20 µm
13　and black carbon (BC) mass concentrations were made across the Indo-Gangetic Plains (IGP), for
14　the first time, from three distinct locations, just prior to the advent of Indian Summer Monsoon over
15　the IGP. These measurements provided an east-west transect of region-specific properties of aerosols
16　as the environment transformed from mostly-arid conditions of western IGP (represented by
17　Jodhpur, JDR) having dominance of natural aerosols to the Central IGP (represented by Varanasi,
18　VNS) having very high anthropogenic emissions, to the eastern IGP (represented by the coastal
19　station Bhubaneswar, BBR) characterized by a mixture of the IGP outflow and marine aerosols.
20　Despite these, the aerosol size distribution revealed an increase in coarse mode concentration and
21　coarse mode mass-fraction (fractional contribution to the total aerosol mass) with increase in altitude
22　across the entire IGP, especially above the well-mixed region. Consequently, both the mode radii
23　and geometric mean radii of the size distributions showed an increase with altitude. However, near
24　the surface and within the atmospheric boundary layer (ABL), the features were specific to the
25　different sub-regions; with highest coarse mode mass fraction (F_{MC} ~72%) in the western IGP and
26　highest accumulation fraction in the Central IGP with the eastern IGP coming in-between. The
27　elevated coarse mode fraction is attributed to mineral dust load arising from local production as well
28　as due to advection from the west. This was further corroborated by data from Cloud Aerosol
29　Transportation System (CATS) onboard International Space Station (ISS), which also revealed that
30　the vertical extent of dust aerosols reached as high as 5 km during this period. Mass concentrations
31　of Black Carbon (BC) were moderate (~1 µg m^{-3}) with very little altitude variation up to 3.5 km,
32　except in the Central IGP (VNS) where very high concentrations were seen near the surface and
33　within the ABL.

34　Keywords: Aerosol size distribution profile, BC mass fraction, aerosol type, IGP, monsoon,
35　SWAAMI

36

37　**Corresponding Author**:
38　　Dr. Mukunda M. Gogoi
39　　Scientist
40　　Space Physics Laboratory, Vikram Sarabhai Space Centre
41　　Indian Space Research Organization, Thiruvananthapuram – 695022, India
42　　Email: dr_mukunda@vssc.gov.in
43　　Phone: +91-471-256 3365; Fax: +91-471-270 6535
44

1. Introduction

45

46 The Indo-Gangetic Plains (IGP) remains one of the global hotspots of aerosols. The prevailing high

47 aerosol loading and the relative abundance of its constituents (being a mixture of natural and

48 anthropogenic species) is known to show significant seasonality (Rana et al., 2019; Vaishya et al.,

49 2018; Brooks et al., 2018; Moorthy et al., 2016; Praveen et al., 2012; Gautam et al., 2011). This

50 arises due to combined effects of the dense population and the associated anthropogenic and

51 industrial activities, as well as the loose alluvial soil of this regions having vast semi-arid and arid

52 characteristics to the west. A dense network of thermal power-plants, several of them being coal

53 fired, is among the prominent source of anthropogenic emissions over the region. This is abetted by

54 the synoptic meteorology with its strong seasonality (Nath et al., 2018; Singh et al., 2018; Gautam

55 et al., 2010) and the orography that slopes down from the west to east bound on the north and south

56 respectively by the Himalayas and the Aravalli ranges and Bihar Plateau forming a confined channel

57 (Moorthy et al. 2007; Gogoi et al., 2017). For accurate quantification of the radiative implications

58 of this complex aerosol system, several concerted studies have been made using ground based

59 (Bansal et al., 2019; Giles et al., 2011) and space-borne measurements (Kumar et al., 2018; Mhawish

60 et al., 2017; Srivastava, 2016) as well as numerical modeling (Govardhan et al., 2019). However,

61 most of these studies have uncertainties arising out of the ill-represented altitude variation of aerosol

62 properties due to sparse measurements. Height resolved in-situ measurements of aerosol properties

63 are indispensable not only in this regard, but also for understanding aerosol-cloud interactions.

64 In recent years, a few campaign-mode airborne measurements have been made over this region to

65 estimate the altitude-resolved properties of aerosols that are important in aerosol-radiation

66 interactions (Gogoi et al., 2019; Vaishya et al., 2018; Babu et al., 2016; Nair et al., 2016;

67 Padmakumari et al., 2013). These include the measurements of aerosol scattering and absorption

68 coefficients conducted as part of the Regional Aerosol Warming Experiment (RAWEX; Babu et al.,

69 2016) to delineate the spatio-temporal variability in the altitude distribution of aerosol single

70 scattering albedo (SSA) across the IGP during winter and pre-monsoon seasons and aerosol and

71 cloud parameter measurements conducted as part of the Cloud Aerosol Interaction and Precipitation

72 Enhancement Experiment (CAIPEEX; Konwar et al., 2015). Some studies have also reported

73 significant contribution of dust and BC as the elevated aerosol load (Pandey et al., 2016; Li et al.,

74 2016; Praveen et al., 2012; Kedia et al., 2014) and their potential role to act as ice nuclei

75 (Padmakumari et al., 2013). However, despite its importance in radiative interactions and CCN

76 activation, the altitude-resolved measurements of aerosol size distribution are extremely sparse, or

77 non-existent, especially just prior to the onset of the Indian Summer Monsoon, when the sources of

78   aerosols, their mixing and transport pathways are all complex. This was among the important

79   information aimed to be obtained under SWAAMI (South-West Asian Aerosol Monsoon

80   Interactions; https://gtr.ukri.org/projects?ref=NE%2FL013886%2F1) - a joint Indo-UK field

81   experiment involving airborne measurements using Indian and UK aircrafts during different phases

82   of the Indian monsoon, right from just prior to the onset of monsoon (i.e. in the beginning of June).

83
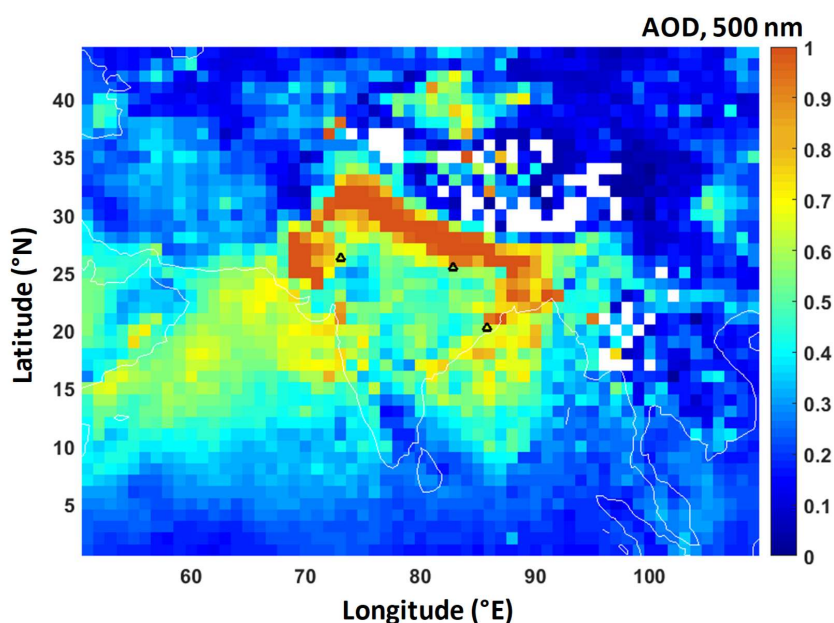
Figure-1: Three distinct base stations: (i) 'Jodhpur (JDR; 26.25°N, 73.04°E)' in the western IGP,

(ii) 'Varanasi (VNS; 25.44°N, 82.85°E)' in the central IGP and (iii) 'Bhubaneswar (BBR; 20.25°N,

85.81°E)' in the eastern coastal IGP, from where the aircraft measurements were conducted during

01-20 June 2016. The background colour is indicative of the mean AOD at 550 nm during the study

period obtained from MODIS sensor (MOD08_D3_6.1, Dark-Target and Deep-Blue combined

mean) on-board Terra satellite.

90   During this campaign, vertical profiles of various aerosol properties have been measured using an

91   instrumented aircraft from three base stations – Jodhpur (JDR), representing the semi-arid western

92   IGP; Varanasi (VNS), representing central IGP characterized by significant anthropogenic activities;

93   and the industrialized coastal location in the eastern end of the IGP (Bhubaneswar, BBR) – during

94   01 to 20 June 2016, just prior to the onset of the Indian summer monsoon. Some important results

95   on the optical and CCN characteristics are already reported (Vaishya et al., 2018; Jayachandran et

96   al 2019). In the present study, we have examined the vertical profiles of aerosol number-size

97 distributions in the size (diameter)regime 0.5 to 20 µm and black carbon (BC) mass concentrations,

98 across the IGP (Figure 1), based on the measurements over western, central and eastern IGP from

99 base stations shown in the figure. The results are presented and discussed in the light of other

100 supplementary information.

101 **2. Experimental Details and database**

102 2.1 Study region and flight details

103 The measurements were carried out aboard the instrumented aircraft (Beechcraft-200) fitted with an

104 iso-kinetic inlet, mounted (front facing) at the bottom of the fuselage for aspirating ambient aerosols

105 and detailed in a few earlier papers (Babu et al., 2016; Vaishya et al., 2018; Gogoi et al., 2019). A

106 constant volumetric flow of 70 LPM (liters per minute) was maintained using an external pump

107 connected to the main inlet assembly, which provided iso-kinetic flow for the average speed of 300

108 km/hr maintained by the aircraft during the entire campaign. The efficiency of this inlet system has

109 been already proven in several previous campaigns (Gogoi et al., 2019; Nair et al., 2016; Babu et

110 al., 2016).

111 The base stations, from where the aircraft operations were carried out, represented distinct regions

112 of the IGP; 'Jodhpur (JDR; 26.25°N, 73.04°E)' in the western IGP is an arid/ semi-arid region with

113 low urban activities, lying downwind the 'Great Indian Desert' to its west (JDR has population

114 density of 161 per sq. km).'Varanasi (VNS; 25.44°N, 82.85°E)' in the central IGP is located

115 downwind of Jodhpur, characterized by extensive anthropogenic activities (automobiles, small and

116 large-scale industries and thermal power plants and wide spread agricultural activities) by its dense

117 population (density 2,399 km^{-2}). 'Bhubaneswar (BBR; 20.25°N, 85.81°E)' is an urban location in

118 the eastern IGP (population density of 2131 km^{-2}), and experiences the influence of marine aerosol

119 component from the Bay-of-Bengal (~ 50 km away from the base station) in addition to the influence

120 of IGP outflow and local aerosol sources from nearby thermal (coal based) power plants, mining and

121 fertilizer based industries etc. (Panda et al., 2016). The northwestern part of India has an undulating

122 topography, due to which monsoon currents loose moisture while crossing the western mountain

123 ranges (Aravalli) and results in dry arid regions (Moorthy et al., 2007). Strong dust-rising winds are

124 a common feature of the IGP in general and its western parts in particular during April to July

125 (Banerjee et al. 2019). In the central IGP, Varanasi and its environs holds largely even topography,

126 where the Ganga is the principal river. In the eastern IGP, BBR is topographically decorated with

127 western uplands and eastern lowlands, with hillocks in the western and northern parts. These base

128 stations, thus provided a west-east cross section of the highly aerosol laden IGP; where the aerosol

129 characteristics are known to change longitudinally. The geographical positions of the three base

130 stations, along with the actual dates of onset of the monsoon at different parts of India in 2016 are

131 shown in Figure 2a.

132
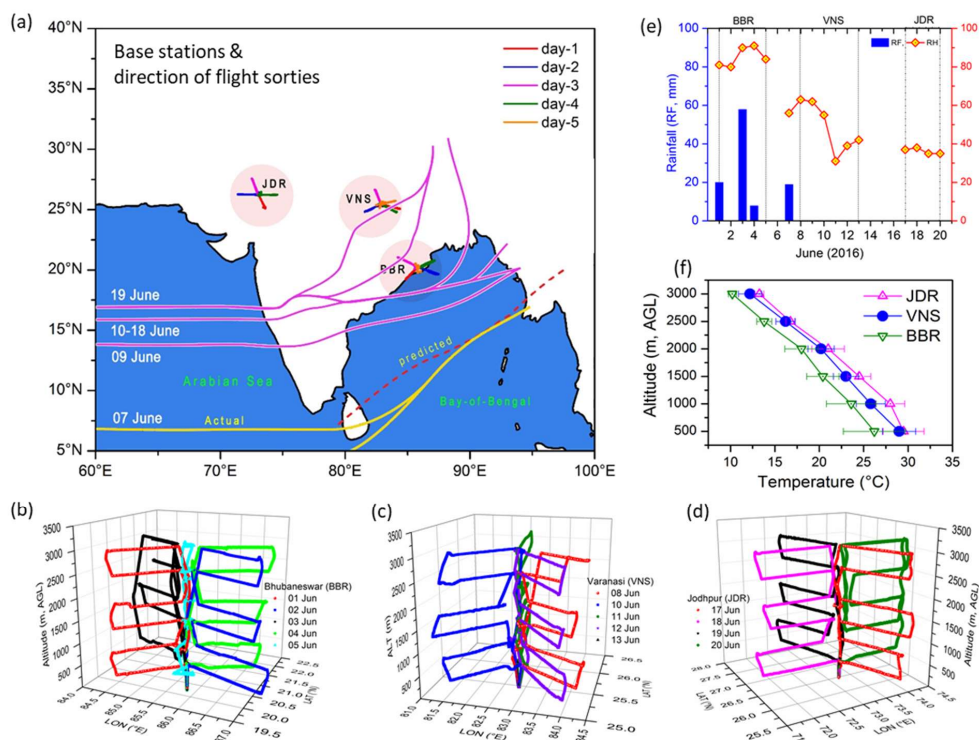
Figure-2: (a) The base stations in the northern part of India. The onset (actual) of SW-Monsoon at different parts of India is also shown in the figure by the yellow and pink (solid) lines. Horizontal and vertical flight paths during each of the sorties at (b) Jodhpur (JDR), (c) Varanasi (VNS) and (d) Bhubaneswar (BBR); (e) Daily rainfall (total) and relative humidity (mean) during the period of observation; (f) vertical profiles of mean ambient temperatures.

138 As can be seen from it, despite a delayed onset at the southern tip of India, monsoon made a fast

139 advance. Yet, all the sorties from the respective base stations were completed well ahead of the

140 advent of monsoon to that station. At the eastern IGP 'BBR', the aircraft sorties were made during

141 01-05 June 2016 when monsoon has not yet set-in over India; at 'VNS', the flights were conducted

142 during 08-13 June 2016, while monsoon has advanced only to the central peninsula. By 19 June

143 2016, the southwest monsoon has covered most of the central and eastern part of India, but yet to

144 progress towards northwester parts and the final set of sorties were conducted at 'JDR' during 17-20

145 June 2016; thereby providing altitude-resolved information on aerosols across the IGP, just prior to

146 the onset of monsoon over the region.

147 From each of the above base stations, 4 to 5 sorties were carried out on successive days in different

148 horizontal directions about the station, as shown by the ground projections (horizontal lines in Fig

149 2a), with a view to obtaining average sub-regional representation in the shortest time possible.

150 During each of the sorties, measurements were made at six discrete levels following a staircase

151 configuration as shown in Figure 2b-d (for JDR, VNS and BBR respectively). Accordingly, the

152 aircraft initially climbed to the base/ ceiling altitude, stabilized and made horizontal flight along the

153 projected track for about 30 min before climbing up/ down to the next higher/ lower levels and

154 stabilizing. This procedure was repeated for all levels (~ 0.5, 1, 1.5, 2, 2.5 and 3 km a.g.l.) until the

155 last level. The ceiling altitude was restricted to 3.5 km based on unpressurised mode of operation of

156 the aircraft. All the flights were carried out around mid-day so that thorough vertical mixing is

157 established by the daytime convective boundary layer eddies.

158 2.2. On-board Instrumentation

159 *Measurement of aerosol size distribution*

160 A factory-calibrated, Aerodynamic Particle Sizer (APS) spectrometer (TSI, Model: 3321) is used

161 for the measurement of aerosol size distribution. It measures size-resolved number concentration of

162 the ambient aerosols in the size range from 0.5 to 20 μm, over 52 channels spaced equally in

163 logarithmic size bins; at a sampling frequency of 1 minute. Aerosol particles in this size range is

164 most important in influencing the optical (scattering and extinction) and CCN and ice nuclei (IN)

165 characteristics.

166 The APS measures the concentration of particles in terms of their aerodynamic diameters by

167 comparing the velocity of particle (controlled by an accelerating flow field) to that of a unit density

168 sphere having same velocity. Particle velocity is estimated from the measurement of time of flight

169 (Mitchell and Nagel, 1999). In the present study a sheath flow at 4 LPM (litres per minute) was

170 maintained against the sample flow of 1 LPM. The instrument automatically adjusts the flow rates

171 with changes in ambient pressure to maintain the specified flow rates. Occasionally, when the

172 aircraft passes through clouds, the aerosol number concentration shot up from the otherwise stable

173 values. Such outliers are removed following 2σ criteria, wherein data points at a particular level

174 lying outside 2σ values of the level-average were removed. The number of such screened out points

175 were <3% of the total. The consistency in the flow was periodically checked each time, before start

176 of measurements from the new base station. Similarly, the optical components and tubing of the

177 system were cleaned immediately after moving to a new base station.

178

179 *Measurement of Black Carbon aerosols*

180 Mass concentration of ambient BC aerosols was estimated using a 7-channel aethalometer (Model:

181 AE-33, Magee Scientific, USA), which measures the attenuation of light that passes through the

182 aerosol laden filter at wavelengths 370, 470, 520, 590, 660, 880, and 950 nm. During the

183 measurement, the aethalometer was set for 50% maximum attenuation to reduce the 'shadowing

184 effect' (Weingartner et al., 2003), a standard mass flow rate of 2 LPM and time base of 1 min. The

185 effect of air pressure variation with altitude on the measurements was corrected following Moorthy

186 et al., (2004) to estimate the true BC mass concentration (M_{BC})

$$M_{BC} = M_{BC}^* \left[\frac{P_O T}{P T_O} \right]^{-1} \tag{1}$$

188 where M_{BC}^* is the instrument measured raw mass concentration of BC at ambient conditions, P_0 and

189 P are the standard and ambient pressure and T_0 and T are the corresponding temperatures. Details of

190 the aethalometer principle, operation, uncertainty involved and error budget are reported in several

191 earlier literatures (Gogoi et al., 2017; Weingartner et al., 2003; Arnott et al., 2005). In general, the

192 instrumental uncertainty ranges from 50% at 0.05 µg m^{-3} to 6% at 1µg m^{-3} (Corrigan et al., 2006)

193 and the uncertainty in the estimation of absorption coefficients is around 10% (Vaishya et al., 2018).

194 2.3. Supplementary data

195 Supplementary data used in this study include aerosol backscattering coefficients and depolarization

196 ratio measured by the *Cloud Aerosol Transportation System* (CATS) aboard the International Space

197 Station (ISS). The CATS is a comprises of an elastic backscatter lidar consisting of two high

198 repetition rate (4-5 kHz), low energy (1-2 mJ) Nd:YVO$_4$ lasers operating at three wavelengths (1064,

199 532, and 355 nm). The receiver subsystem consists of a 60 cm telescope having a 110 micro-radian

200 field of view, photon-counting detectors, and associated control electronics (Yorks et al., 2014;

201 2016). As the altitude of ISS orbit is about 405 km (51-degree inclination), CATS provides a

202 comprehensive coverage of the tropics and mid-latitudes, with nearly a three-day repeat cycle. Level

203 2 data of CATS (https://cats.gsfc.nasa.gov/data/) are used (Lee et al., 2018) in the present study,

204 which provides the geophysical parameters, such as the vertical feature mask, profiles of cloud and

205 aerosol properties (i.e. extinction, particle backscatter), and layer-integrated parameters (i.e. lidar

206 ratio, optical depth). In addition, types of aerosols are also derived based on CATS typing algorithms

207 where eight aerosol types (in CATS mode 7.1) are identified: volcanic, dust, dust mixture,

208 clean/background, polluted marine, marine, polluted continental and smoke. Incorporating the

209 information of backscatter color ratio (1064/532-nm) and spectral depolarization (ratio of

210 perpendicular to parallel backscatter) ratio (1064/532-nm), Mode 7.1 provides the characteristic of

211 aerosol regimes (York et al., 2016) as below:

212 **Table-1**: Classification of aerosol types for CATS mode 7.1 (York et al., 2016).

Aerosol Type	Aerosol feature base	Depolarization ratio (δ'_{1064})	Color Ratio (γ'_{1064})
Volcanic	> 10 km	-	-
Dust	< 10 km	> 0.3	-
Dust mixture	< 10 km	$0.2 > \delta > 0.3$	-
Clean/background	< 10 km	-	< 0.0005 sr^{-1}
Polluted marine	< 10 km	$\delta'_{1064}/ \delta'_{532} > 50\%$	$\gamma'_{532}/ \gamma'_{1064} < 1.75$
Marine	< 10 km	$\delta'_{1064}/ \delta'_{532} < 50\%$	$\gamma'_{532}/ \gamma'_{1064} < 1.75$
Polluted continental	< 10 km	$\delta'_{1064}/ \delta'_{532} > 50\%$	$\gamma'_{532}/ \gamma'_{1064} > 1.75$
Smoke	< 10 km	$\delta'_{1064}/ \delta'_{532} < 50\%$	$\gamma'_{532}/ \gamma'_{1064} > 1.75$

213

214 2.4. General synoptic meteorology during the campaign

215 The general surface meteorological conditions across the IGP during the campaign period are shown

216 in Figure 2(e-f), while the synoptic conditions are shown in Figure 2(a). The daily mean values of

217 relative humidity (Figure 2e) showed spatial variation typical to this region; varying from very high

218 value (above 80%) at the eastern IGP (BBR) to the lowest value (~ 40%) at the western arid region

219 (JDR), with values varying between 40% and 60% at VNS. The large value of relative humidity

220 (RH) at BBR was also associated with mild pre-monsoon rainfall (Figure 2e) there during the first

221 (01-June-2016; light rain during noon), third (03-June-2016; heavy rain ~ 60 mm in the night) and

222 fourth (04-June-2016; light rain in the morning and during noon) days of observations. Similar to

223 RH, ambient temperature (Figure 2f) also showed spatial variation being warmest at JDR followed

224 by VNS and BBR, throughout the altitude range from the surface to ~ 3 km.

225

Atmospheric
Chemistry
and Physics
Discussions

226 **3. Results and discussion**

227 3.1 Aerosol number size distributions

228 Aerosol number size distributions [dN/d (logDp)], representative of each of the 3 sub-regions of

229 IGP, are presented in Figure 3; the panels from left to right representing the sub-regions JDR, VNS

230 and BBR, from the west to east IGP.
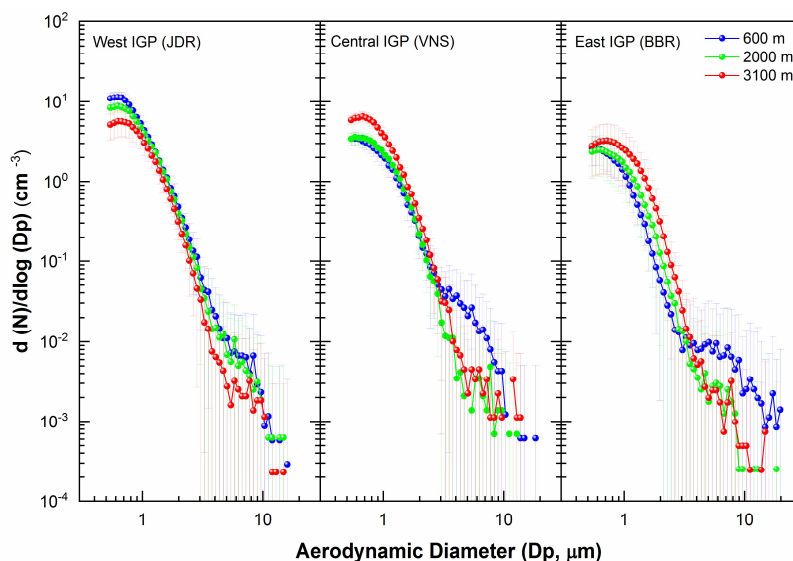
231

232 **Figure-3:** Aerosol number size distributions (mean profiles averaged for all the days) at three

233 distinct altitudes of JDR, VNS and BBR, representative of (i) near the surface (600 m above ground

234 level) having proximity to emission sources, (ii) in the upper ABL (2000 m above ground level) and

235 (iii) in the free troposphere (3100 m). Vertical bars over the points are the ensemble standard

236 deviations. Individual size distributions at different heights of ~ 500 m interval are given in

237 supplementary figure-S1.

238 Three distributions are shown for each station, representative of (i) near the surface with proximity

239 to emission sources (600 m AGL), (ii) in the upper ABL (2000 m AGL) and (iii) in the free

240 troposphere (3100 m AGL) following the mean ABL heights (1.3 ± 0.5 km, 2.3 ±0.5 km and1.4 ±

241 0.2 km for JDR, VNS, and BBR respectively; Vaishya et al., 2018) at local noon time. Aerosol

242 number concentration below 0.542 μm are not size-classified and represented as a single count

243 (between 0.3 and 0.542 μm) are shown as a function of altitude in figure 4 (a).

244   The figures clearly reveal that over all altitudes and at all the stations, the size distributions are

245   consistently bimodal, with a prominent accumulation mode (<1µm) and a weaker secondary mode

246   (>1µm). The concentration of particles in the unclassified size regime (below 0.542 µm), showed a

247   gradual decrease with increase in altitude at all stations and a spatial distinctiveness with highest

248   near surface concentration in the Central IGP (most anthropogenically impacted sub-region of the

249   IGP) depicting sharper altitude variation as against the other two sub-regions.
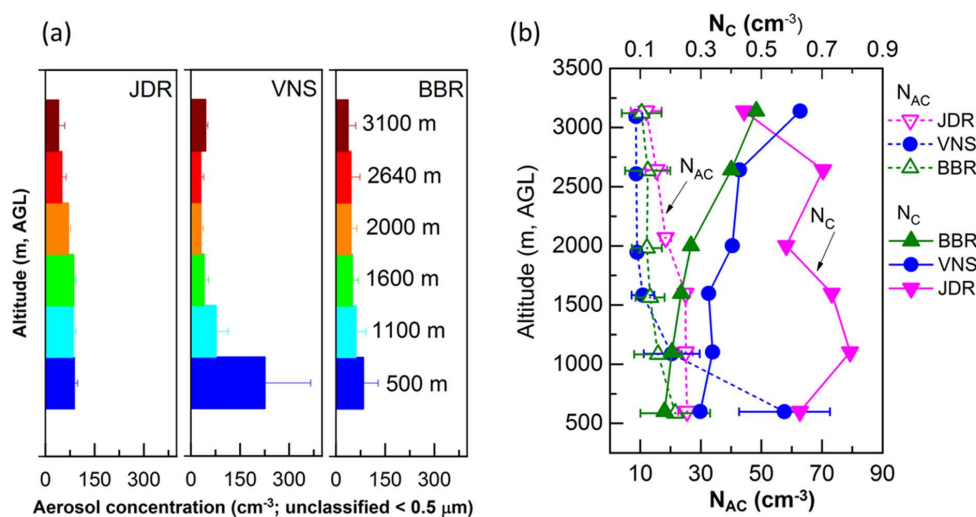
251   **Figure-4:** (a) Aerosol concentrations in the unclassified size range (between 0.3 and 0.54 µm); (b)

252   Vertical profiles of aerosol accumulation and coarse mode number concentrations (N_{AC}) as measured

253   by APS in the accumulation and coarse mode size range (between 0.3 and 20 µm) along with coarse

254   mode number concentrations (N_C).

255   As it is well-established that during pre-monsoon/ prior to the onset of monsoon, both the natural

256   and anthropogenic aerosol species coexist in large abundance over the IGP, we examined in Figure

257   4b, the altitude profiles of accumulation mode aerosols (concentration below 1 µm), which are

258   mostly attributed to be of anthropogenic origin and coarse mode aerosols (above 1 µm), which are

259   mostly of natural origin. Accumulation mode aerosol concentration showed only weak altitudinal

260   dependence above 1 km at all the sub-regions, though at VNS, there was a sharp increase in the

261   concentration below 1 km, obviously due to source-proximity. This feature is seen in Figure 4a also.

262   This observation is supported by the collocated measurements of aerosol total number concentrations

263   (N_T) as measured by a condensation nuclei (CN) counter aboard the aircraft (Jayachandran et al.,

264   2019) in the size range above 2.5 nm, showing highest values of N_T in the entire altitude range of

265   measurements over VNS. On the other hand, the vertical profiles of coarse mode aerosols

266   concentrations (N_C) showed significantly large abundance over the western IGP (arid/ semi-arid

267   regions) represented by JDR, similar to the spring time observations reported by Gogoi et al., (2019).

268   Another interesting feature is the increasing concentration of these coarse mode particles with

269   increase in altitude across the entire IGP; which is most conspicuous at the central IGP and least at

270   the west, implying their increasing role at higher altitude; probably due lofted regional dust and

271   advected mineral dust from west Asian regions.

272   With a view to quantifying this, the size distribution spectra are averaged for each altitude level and

273   for each station. From these spectra, the geometrical mean diameter (Dg) is estimated as a function

274   of altitude, using the following equation

275
$$D_g = exp\left[\frac{\sum_l^u n_i\, ln(D_{pi})}{N}\right] \tag{2}$$

276   where $D_{pi}\left(= \sqrt{(D_i * D_{i+1})}\right)$ denotes the geometric midpoint of each channel of the APS, n_i is the

277   particle concentration in i^{th} channel and $N = \sum_l^u n_i$ is the total concentration. Accordingly, Dg of a

278   spectrum of particles is the 50% probability point of an equivalent diameter having half of the

279   particle concentrations larger than this size and remaining half below that. The vertical profiles of

280   Dg and mode $\left(= D_p(n_{max})\right)$ of the distributions are shown in Figure 5. It clearly shows the increase

281   of the coarse mode fraction in the size distribution; with both the mode and Dg showing a steady

282   increase with altitude; especially Dg. The rate of increase of Dg with altitude increases from west to

283   east across the IGP, being highest at BBR (Figure 5b). In the central IGP where mixed aerosol type

284   prevails, the increase in Dg within the ABL is rather weak, but in the free troposphere it increases

285   more sharply probably due to the faster decrease in the accumulation mode concentration (Figure 4)

286   or the prevalence of advected dust at higher altitudes or both.

287   The observations that have foregone reveal the non-uniform distribution of dust and anthropogenic

288   sources of aerosols. Nearly steady values of N_C in the entire column at JDR are attributed to the

289   strong convective mixing over this region associated with intense solar heating during summer when

290   the surface temperatures are above 40° C (Vaishya et al., 2019). On the other hand, altitude variation

291   of accumulation and coarse mode aerosols are relatively more fluctuating at BBR and VNS,

292   compared to that at JDR (Figure 4b).
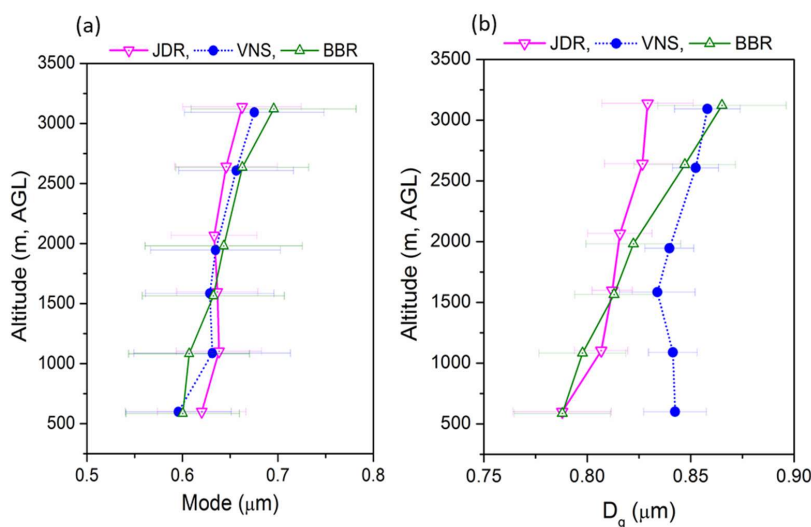
Figure-5: Vertical profiles of (a) mode and (b) geometric mean diameters (Dg) of aerosol number size distributions at different heights above the ground level, indicating the change in the pattern of distribution with altitude and from the western to the eastern part of India.

These observations are also in-line with the reported values of dust fractions (Vaishya et al., 2018) during the same campaign, showing the enhancement of dust fraction from 10 to 20 % at 300 m to close to 100% above 2 km altitude at JDR; while smallest dust faction (< 10%) was observed at BBR. Over the central IGP, synoptic wind-driven desert dust aerosols, leads to elevated layers of aerosols having higher dust fraction (>50%). However, it should be noted that dust over the central IGP is more absorbing in nature because of its mixing with other anthropogenic emissions (such as BC; Vaishya et al., 2018), while that over western IGP is rather pristine in nature. Thus, quantification of the absolute magnitude of coarse mode aerosol concentrations is very important to understand the significance of elevated aerosol load on radiative perturbations, because coarse mode dust contributes largely to aerosol scattering as well as absorption, compared to their anthropogenic counterpart, which contributes dominantly to absorption.

Apart from the number-weighted expression of aerosol size distributions, the mass-weighted distributions carry useful information for quantifying regional distinctiveness of the dominance of coarse mode particles. Even though the fine mode aerosols are extremely numerous in the atmosphere and important for microphysical processes, they represent only a very small proportion of total particle mass; whereas coarse mode particles, even though far less numerous, have significant mass/ volume. In simple terms, particle number concentrations are dominant in the fine

314   mode (< 0.1 μm), the surface area is predominantly in the accumulation mode (0.1 to 1 μm), and the

315   volume, and hence mass, is divided between the accumulation mode and coarse particle mode. In

316   the present study, since the size range of particle counts are confined in the accumulation and coarse

317   mode regimes (between the 0.5 and 20 μm), quantitative picture of aerosol mass concentrations is

318   obtained by assuming a uniform density equal to 2 g cm^{-3} following Moorthy et al., (1998), Pillai et

319   al., (2001). Since the size-resolved particle densities are not known, we did not use effective density

320   (mass-mobility relationship defined as the mass of the particle divided by its mobility equivalent

321   volume) of particles to calculate the mean particle mass size distributions.

322
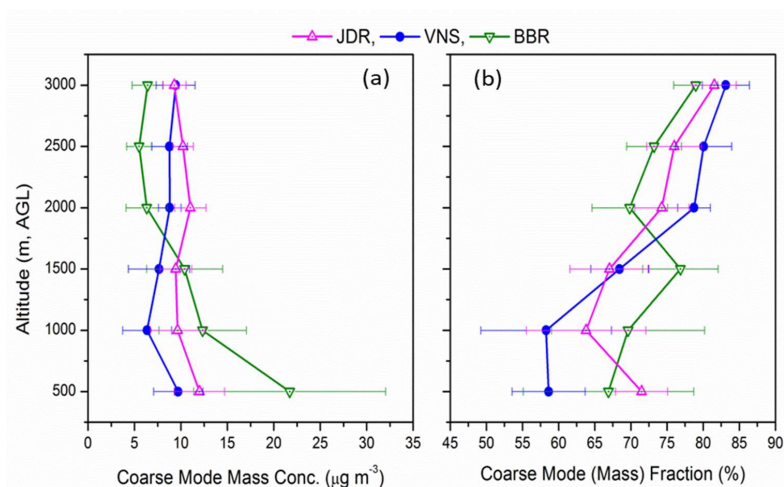
Figure-6: (a) Vertical profiles (mean and standard deviations) of coarse mode aerosol mass concentrations (M_C). The values are derived from the aerosol number concentrations at different size bins, assuming a density of 2 gm/cm^3; (b) Vertical profiles of aerosol coarse mode fractions (F_{MC}) at different locations.

Figure 6a shows the altitudinal variation of coarse mode aerosol mass concentrations over all the observational sites, along with the values of coarse mode mass fractions (F_{MC}). Over VNS and JDR, consistently higher values of M_C were seen in the entire altitude range. This is in line with the higher values of coarse mode aerosol concentrations (N_C) at these sites, JDR being the highest. On the other hand, the values of M_C at BBR decreased significantly from the surface to lower free-tropospheric region. The higher values M_C observed near the surface at BBR can be attributed to the influence of local sea-salt aerosols; however not affecting the values of Dg as there may present significant abundance of accumulation mode aerosols over this site remaining beyond the detection limit of APS.

336   Similar to that of N_C, F_{MC} showed (Figure-6b) gradually increasing values with altitude at all the

337   locations. The high values of coarse mode mass fraction and an increasing trend with altitude is

338   indicative of the role of upper level transport of dust from the western desert regions, in addition to

339   those contributed locally due to thermal convective processes. As compared to other two stations,

340   highest value of F_{MC} (~ 70%) near the surface was seen at JDR indicating the role of arid nature of

341   the region. This exercise clearly explains the abundance coarse mode dust decreasing from west to

342   east; along with an increase in the contribution of anthropogenic fine/ accumulation mode aerosols.

343   With a view to examining transport of mineral dust (by the synoptic winds) the spatial distributions

344   of UV-aerosol index, aerosol types and aerosol absorption optical depth (AAOD); all derived from

345   the Level-3 OMAERUVd data product (daily, 1.0 degree x 1.0 degree) from Ozone Monitoring

346   Instrument (OMI, on-board Aura satellite; Levelt et al., 2006), are examined. OMAERUV uses the

347   pixel level Level-2 Aerosol data product of OMI at three wavelengths (355 nm, 388 nm and 500 nm)

348   to derive AAOD. Higher values of AAOD at 388 nm are indicative of the presence of dust or biomass

349   burning aerosols, as dust and organic carbon being strong absorbers of UV radiation. As the period

350   this campaign was devoid of major fire activities over the study region (northern India) which

351   normally peaks in April to May and October to November, corresponding to burning after the wheat

352   and rice harvests (Vadrevu et al., 2011; Venkataraman et al., 2006), the AAOD values would be

353   representative of dust loading. This aspect is conformed in a subsequent section using lidar

354   depolarization ratio.

355   Figure 7a-d shows the spatial distributions of UV aerosol index, aerosol type and AAOD at 388 nm

356   and 500 nm, while the synoptic winds are shown in Figure 7e. A very good association between the

357   westerly advection and dust loading extending from west to central IGP is noticeable from the figure.

358   This lends further support to the role of advected dust leading to higher M_C and F_{MC} at higher

359   altitudes, seen in figures 6. In this context, it is also worth noticing that based on observational data

360   and regional climate modeling, Banerjee et al., (2019) have clearly shown (in their Figure 7) the

361   significant vertical extent of dust loading, both of local and remote origin, during pre-monsoon and

362   summer across the IGP reaching altitudes as high as 600 hPa.

363

364
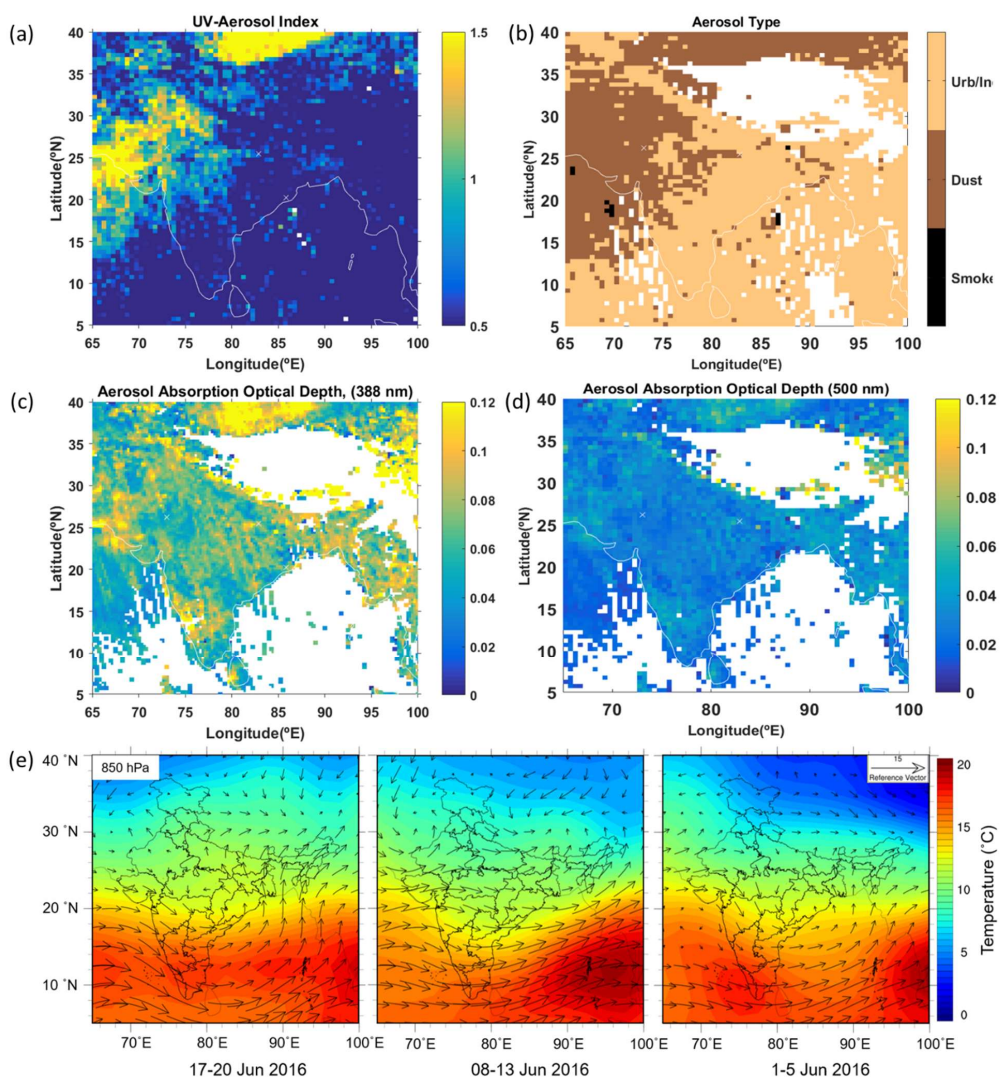
Figure-7: Spatial distribution of (a) UV aerosol index, (b) aerosol type, (c) aerosol absorption optical

depth (AAOD) at 388 nm and (d) AAOD at 500 nm during June 2016 (geographic positions being

shown by the 'x' marks). (e) Synoptic wind and temperature at 850 hPa.
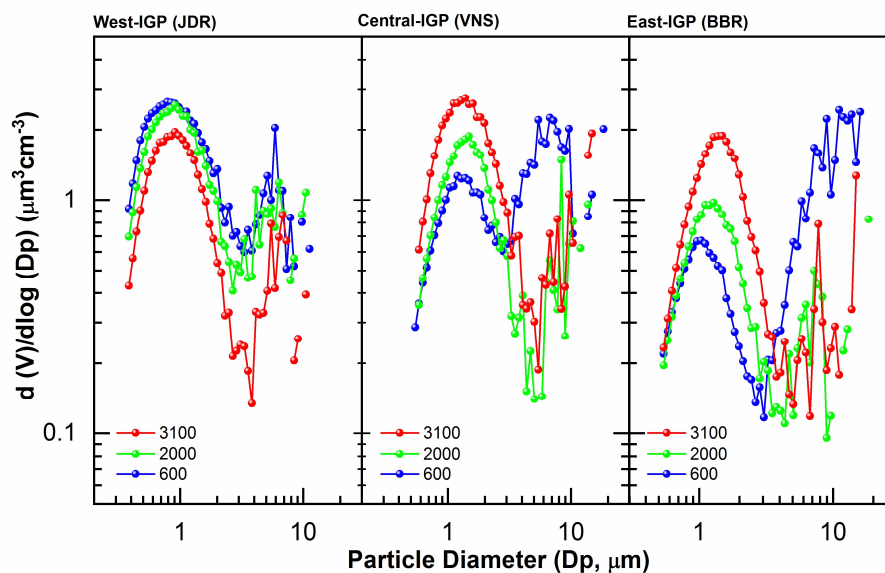
Figure-8: Aerosol volume size distributions (mean profiles averaged for all the days) at distinct three distinct altitudes (600 m, 200m and 3000 m) of the atmosphere (shown by different color) over JDR, VNS and BBR.

The volume size distribution of aerosols (shown in Figure 8) at three distinct altitude regions of the atmosphere also clearly shows the altitudinal change in the pattern of distribution, changing from coarse mode dominance near the surface to accumulation mode dominance at the ceiling altitude over BBR. While those at JDR, the pattern of distributions remains same in the entire column. Similar to JDR, VNS also depicted significant enhancement in coarse mode aerosols in the upper levels (at 2 and 3 km altitudes) of the atmosphere. Similar to these observations, based on the collocated spectral scattering properties of aerosols obtained during the same experiment, Vaishya et al., (2018) have reported that, as we move from west to east in the IGP, the aerosol population changes from super-micron mode dominant natural aerosols to sub-micron mode dominant anthropogenic aerosols. Moreover, large abundance of coarse particles (>2µm) along with significant fine/ accumulation mode aerosols in the column highlights the complex mixture of dust with other anthropogenic components in all the three regions, making a complex scenario for aerosol radiation and aerosol cloud interaction processes. Based on the combination of satellite remote sensing and regional climate model simulations, Banerjee et al., (2019) have also shown the presence of dry elevated layer of dust (at altitudes between 850 and 700 hPa; taking place in multiple layers)

Atmospheric
Chemistry
and Physics
Discussions

387   during June across the IGP, transported from the Thar Desert to the northern Bay-of-Bengal. To

388   ascertain this further, we have examined the data from CATS aboard ISS.

389   3.2 Inferences from the CATS data

390   Geophysical parameters derived from the CATS on board ISS are very useful to infer on aerosol

391   features in the atmospheric column, especially at altitudes above the ceiling altitude of the aircraft

392   (3.1 km). In the present study, we have considered three products from CATS for the campaign

393   period, viz. (i) depolarization ratio, (ii) attenuated backscatter coefficients and (iii) aerosol types.
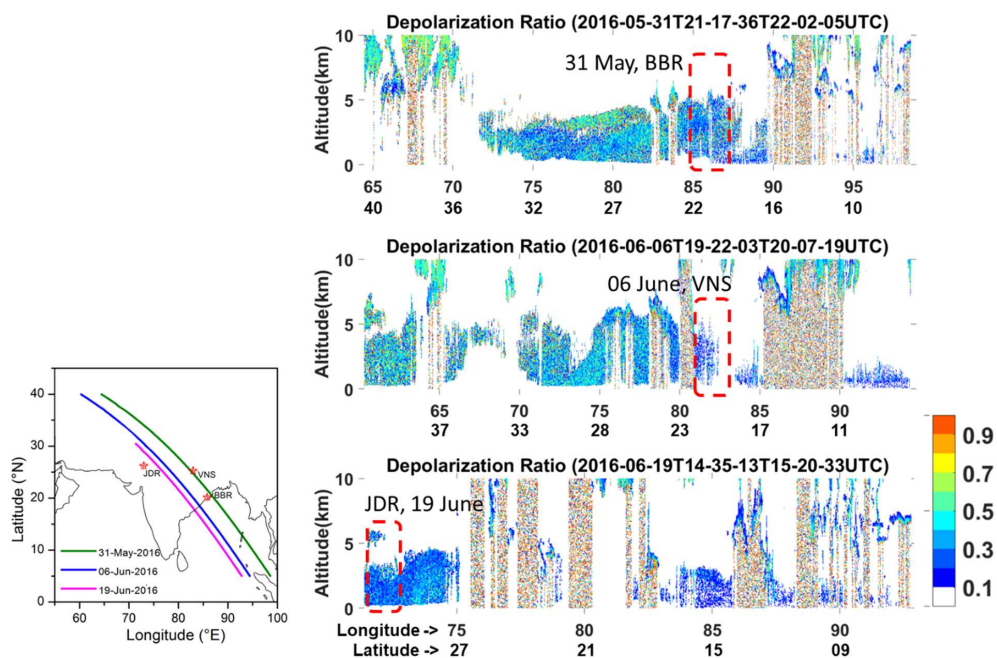

394

395   **Figure-9:** Aerosol Depolarization Ratio [obtained from Cloud Aerosol Transportation system in

396   International Space Station (ISS)] for three different passes of the ISS over the three sub-regions

397   during the period of aircraft observation. The tacks of the CATS are shown by the solid lines in the

398   left panel and the rectangular boxes in the right panels show the data over the sub-regions.

399   Figure 9 shows the vertical cross-section of depolarization ratio for three passes during the campaign

400   period and close to the three sub-regions (identified by the rectangular boxes in the figure). Higher

401   values (~0.3) of depolarization ratios are seen in the western IGP (JDR, bottom panel), suggesting

402   the dominance of non-spherical (dust) particles. The depolarization ratio decreases towards east

across the IGP, with values in the range 0.2 and 0.3 at the central IGP, and further 0.2 and 0.1 in the eastern site BBR. These lend additional support to the inference on the influence of dust aerosols during the campaign period. Supporting the patterns of depolarization ratio, aerosol types (from CATS mode 7.1) in Figure 10a indicate significant presence of dust at JDR, while the aerosol types over VNS and BBR are mixture of dust, polluted continental and carbonaceous aerosols. Vertical profiles of total attenuated backscatter coefficients show the vertical extent of the aerosol layer to be as high as 5 km (as has been shown by Banerjee et al 2019) over all the sites (Figure 10b).
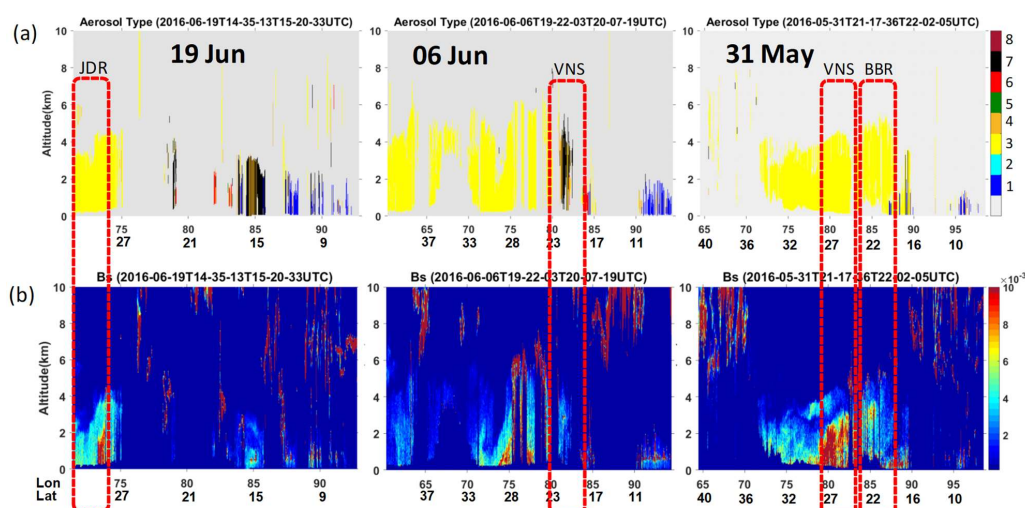
Figure-10: Transects of (a) Aerosol types (1- Marine, 2- Marine Mixture, 3- Dust, 4- Dust Mixture, 5- Clean/ Background, 6- Polluted Continental, 7- Smoke, 8- Volcanic), and (b) Backscatter coefficients (Bs, km^{-1}Sr^{-1}) at 1064 nm obtained during the period of aircraft observation corresponding to the overpass of the ISS.
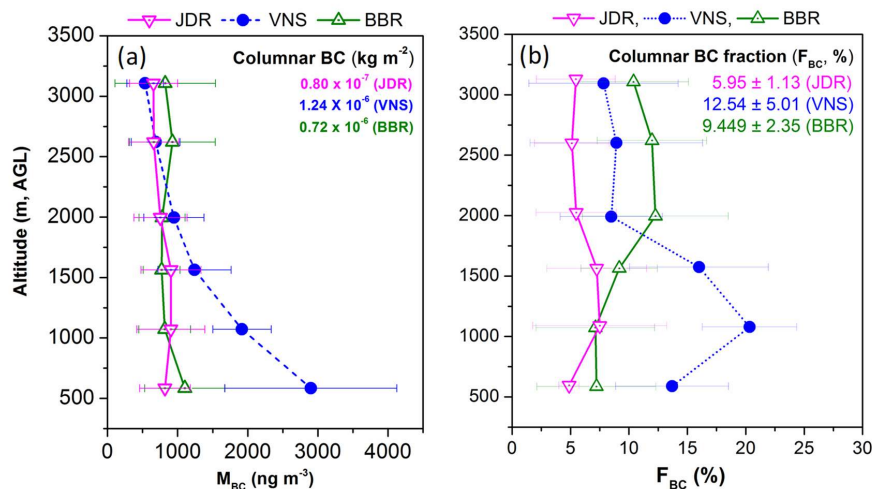
3.3 Vertical profiles of BC

BC is the chief anthropogenic absorbing aerosol species, and the IGP is known to be among the global hotspots (Govardhan et al., 2019). The height resolved information on F_{BC} is important not only in radiative forcing, but on CCN activation as well (Bhattu et al., 2016). Collocated measurements of BC during SWAAMI have been used to examine the vertical profiles of BC and its variation across the IGP prior to the onset of Indian summer monsoon. Figure 11a shows the vertical profiles of BC for the three sub-regions. Each profile is the average of all the profiles

Atmospheric
Chemistry
and Physics
Discussions
Open Access
EGU

423 obtained from measurements made from each of the base station. It is seen that, BC remained low

424 (~1 µg m^{-3}) and depicted very weak altitude variations at the western and eastern IGP regions (JDR

425 and BBR), while in the central IGP (VNS) there is a rapid decrease of BC from the high value (~ 3

426 µg m^{-3}) near the surface. Above 2 km, all the profiles overlap though a weak increase is indicated

427 over BBR, which is examined later. The very high values of BC close to the surface at VNS are

428 attributed to the wide-spread anthropogenic activities in the Central IGP including the cluster of

429 thermal power plants in that region. Consequently, the columnar concentration of BC (integrated up

430 to 3 .1 km) is also the highest at VNS.

Figure-11: (a) Vertical profiles of the mean values of BC mass concentrations (M_{BC}) and BC mass fractions (F_{BC}) at JDR, VNS and BBR. (b) Daily profiles of M_{BC} during each of the flight sorties on different days.

435 However, the vertical profiles of the fractional contribution of BC (F_{BC}) to the total composite

436 aerosol mass (estimated from the volume size distribution, considering a uniform density of 2 gm/cc,

437 especially in view of the abundance of dust) shows (Figure 11b) sub-regional distinctiveness. It

438 remains the lowest (~ 6%) in the western IGP, with very little altitude variation. In the central IGP,

439 F_{BC} is quite high (~15 % to 20%) within the ABL and drops of fast above 2 km approaching the

440 values seen for the western IGP. F_{BC} depicts an elevated peak at around 1 km above ground level at

441 VNS, while at BBR, higher F_{BC} values occur at still higher altitudes at BBR, where the near-surface

442 values are much lower and comparable to those at JDR. There is a steady increase in F_{BC} from near

443 surface to higher altitudes, and above 2 km, the values are comparable to the peak values seen at

444 VNS (at ~ 1 km altitude). Despite this, the integrated BC concentration comes in between those of

445   JDR and VNS, mainly because of the large values occurring in the lower atmosphere at VNS. It may

446   be recalled that based on SWAAMI aircraft measurements, Vaishya et al., (2018) have reported that

447   while the scattering characteristics remained uniform across the IGP, the absorption coefficients

448   showed sub-regional distinctiveness, leading to a west to east gradient (decrease) in the vertical

449   structure of single scattering albedo (SSA).

450   Investigation of the vertical profiles of BC mass concentrations on individual days (Supplementary

451   Figure-S2) helps to see the distinctiveness at each sub-region, resulting from the spatially

452   heterogeneous nature of emission sources and advection, especially at BBR where the inland

453   profiles, made during sorties perpendicular to the coastline (on 2nd and 3rd June) show significantly

454   higher values of BC at higher altitudes than those along the coastline. At BBR, this arises mainly

455   because of source impacts that are spatially heterogeneous. The regions towards northwest of BBR

456   are characterized by large scale urban and industrial activities (Ambient air quality status and trends

457   in Odisha: 2006 - 2014). Similarly, near surface BC concentrations at VNS was higher when the

458   flight sorties were confined to NE, NW and SW of the city Centre, while the values in the SE sector

459   was lower. On the other hand, at JDR, the profiles revealed a better spatial homogeneity.

460   In this context, we have examined the possible role of the large network of thermal power plants

461   (TPP) over the northern part of India, which is reported to significantly contribute to regional

462   emissions (Singh et al., 2018). These include the emissions of CO_2, NO_2, SO_2, soot, suspended

463   particulate matter (SPM) and other trace gas species. More than 70% of the thermal power plants

464   over the IGP are coal based and CO_2 and SO_2 hold more than 47% of the total emission share. As it

465   is not possible to measure soot from space, to infer on the role of these emissions from thermal power

466   plants in causing the higher BC fraction at higher attitude over BBR, we have examined the spatial

467   distribution of the concentrations of the co-emitted NO_2 and SO_2 in Figure 12, in which the locations

468   of major thermal power plants (TPP) are also marked. The data are obtained from OMI onboard

469   AURA satellite. Higher concentrations of NO_2 and SO_2 are readily discernible from the figure around

470   the regions (marked in the figure) where there are clusters of thermal power plants. As the energy

471   consumption is the highest during summer and most dependent on thermal, these TPP should be

472   operating to near full capacity. This provides an indirect support to the high concentrations of BC

473   (co-emitted) at higher levels. In general, these TPPs have tall stacks (heights in the range 200 to 400

474   m) and aids easy ventilation to the lower free-tropospheric altitudes.

Atmospheric
Chemistry
and Physics
Discussions

Open Access

EGU

475
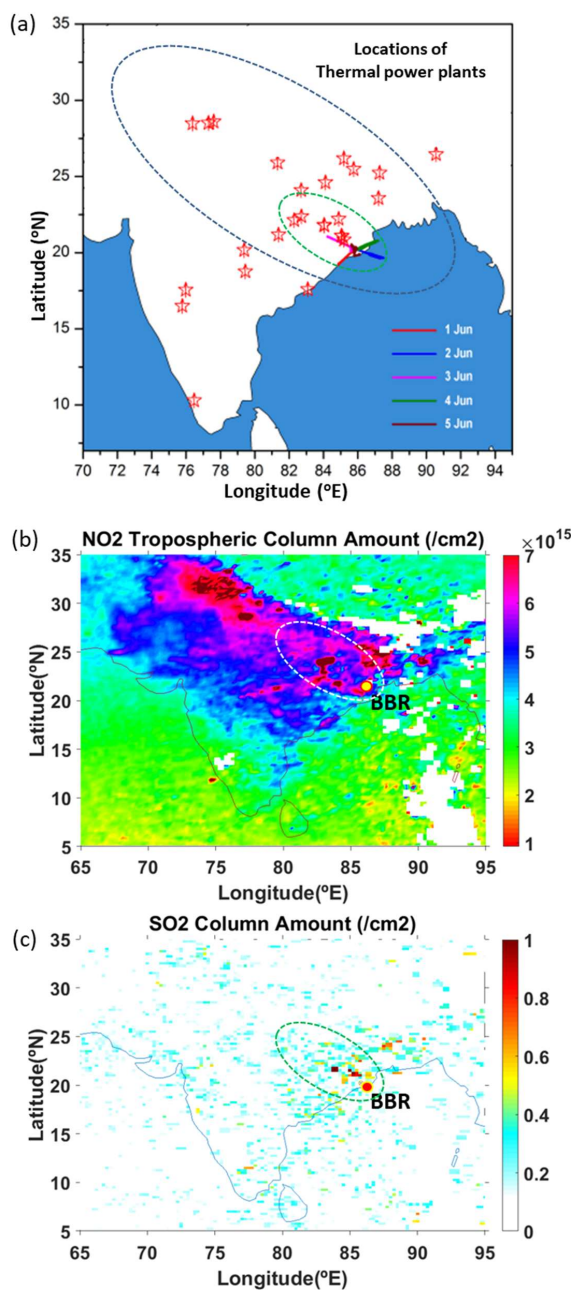
Figure-12: (a) Geographic position of thermal power plants (TPP) over India (the TPP across the
IGP are bounded by the blue dashed line, and those along the flight direction of BBR are bounded
by the green dashed line), along with the spatial map of tropospheric column abundance of (b) SO_2
column amount (DU) and (c) NO_2 (/cm^2) over the northern part of India..

Atmospheric
Chemistry
and Physics
Discussions
Open Access
EGU

480 To further ascertain this, the spectral properties of aerosol absorption are examined. First, we have

481 examined the frequency distribution of Ångström absorption exponent (α_{abs}, derived from the linear

482 fit on log-log scale between corresponding absorption coefficients to aethalometer wavelengths) in

483 Figure 13; separately for the mixed layer (ML, below 1.5 km) and above (≥2km). The frequency

484 distribution of α_{abs} reveals a clear shift towards lower values as we move from JDR to BBR, both

485 within the ML and above, even though the values of α_{abs} lying mostly between 1 and 1.5. Based on

486 laboratory studies and field investigations, it has already been shown that the higher values of α_{abs}

487 (~ 2) are representative of biomass burning emissions, while the values ~ 1 are indicative of fossil

488 fuel combustions (Kirchstetter et al., 2004).
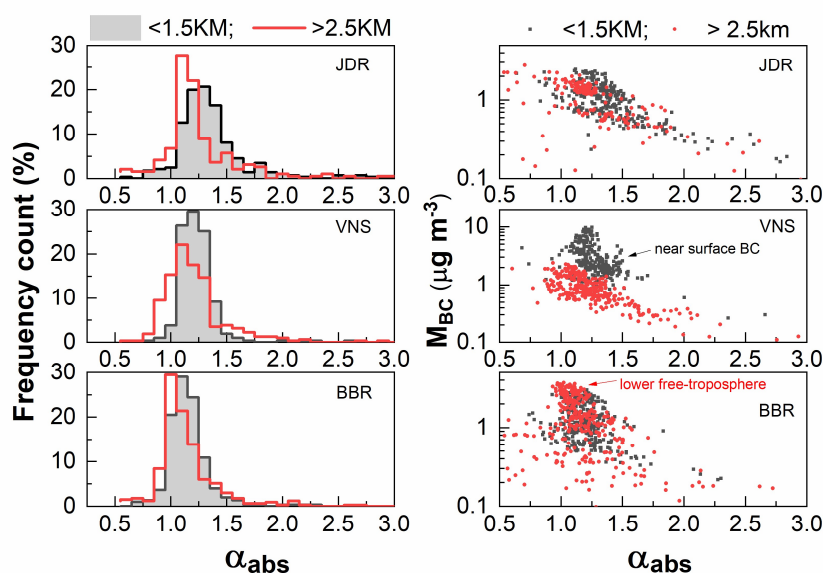
489

490 **Figure-13:** (a) Frequency of occurrences of Angstrom absorption exponent (α_{abs}) below 1.5 km and

491 above 2.5 km altitude, (b) variation of BC mass concentrations corresponding to different values of

492 α_{abs} are shown in the right panels for the same two altitude regimes at distinct locations of northern

493 India.

494 Examining Figure 13 in the above light, it emerges that significant contribution of BC of fossil fuel

495 origin prevails at higher altitudes over BBR, while the association between the two decreases

496 abruptly from ML to higher height at VNS. The consistent higher values of BC in the column

497 associated with the values of α_{abs} lying between 1 and 1.5 are indicative of influence of

498 anthropogenic sources at BBR. This can also be due to the aging of BC at higher heights, during

499 which BC mixes with other species and its angstrom exponent increases, as the spectral dependence

500   of absorption steepens when BC (even though its source could be fossil fuel) is coated with a

501   concentric shell of weakly absorbing material (Gogoi et al., 2017). Further investigations are needed

502   in this direction.

503   3.4 Finds from the present study Vs results reported for other seasons

504   The spatial variation of the altitude profiles of N_{AC}, Dg, F_{MC} and F_{BC} across the IGP hints to several

505   possible implications of their direct and indirect effects. Altitudinal increases in the values of Dg

506   and F_{MC} along with depolarization ratios are indicative of the presence of dust (> 4 μm) in the lower

507   free troposphere, which is known to produce long-wave (warming) radiative effect (Miller et al.,

508   2006; Tegen and Lacis, 1996). Conversely, significant abundance of accumulation mode aerosols,

509   in general, might contribute significantly to scattering. Based on air-borne measurements during

510   SWAAMI, Vaishya et al., (2018) have reported that the values of SSA varied between 0.935 (at 550)

511   in spring to 0.84 (at 530 nm) during pre-monsoon period, indicating a seasonal change in the aerosol

512   type and consequently their optical properties. For example, a clear seasonal change in the vertical

513   profiles of N_{AC} is noticeable at JDR, changing of the much steeper variation (vertically) in winter

514   (as reported by Gogoi et al., 2019) to a near-steady one during just prior to the onset of monsoon

515   (Figure 14).
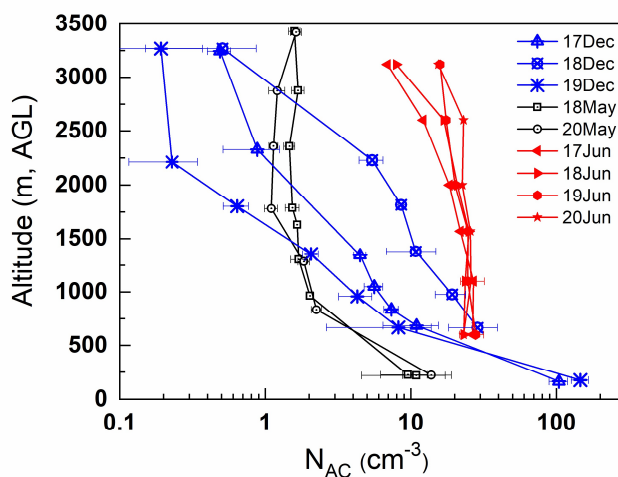
516

517   **Figure-14:** Vertical profiles of seasonal mean values of aerosol accumulation and coarse mode

518   number concentrations (N_{AC}) at Jodhpur during winter-2012 (17-19 Dec), spring-2013 (19 and 20

519   May) and just prior to the onset of monsoon-2016 (17-20 June).

520   To examine the role of the changing synoptic meteorology during this period, we have shown the

521   profiles of vertical velocity (in pressure coordinates from 1000 hPa to 100 hPa) in Figure 15. These

522   are obtained from ERA-interim reanalysis data sets. Here, the positive and negative signs of vertical

523   velocity (ω) are indicative of updraft (as indicated by -ve values of ω) and downdraft (as indicated

524   by +ve values of ω). A clear seasonal transformation is seen, with increasingly stronger updrafts

525   dominating over the IGP from December to June, with the intensity increasing from west to east. In

526   the western IGP regions, the sign of vertical velocity is seemed to change from December to June,

527   progressively enhancing the magnitude of deep convection towards the onset of monsoon imparting

528   stronger vertical dispersion and more homogeneous distribution of aerosols in the column.
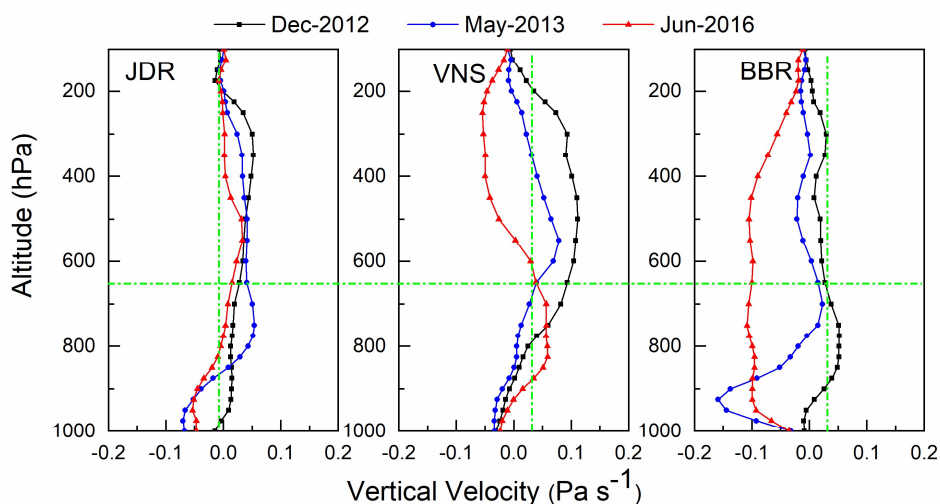
529

530   **Figure-15:** Vertical profiles of vertical velocity (Pa s^{-1}) over the study locations representing Winter

531   (December, 2012), Spring (May, 2013) and just prior to the onset of Monsoon (June, 2016) at

532   different pressure levels from 1000 to 100 hPa. The positive and negative values are indicative of

533   the descending and ascending motions respectively. The horizontal dashed line indicated the ceiling

534   altitude (~ 3.5 km above ground level) of aircraft measurements.

535   The above feature is more prominent over the eastern IGP -'BBR', where the magnitude of vertical

536   velocity is consistently higher from surface to upper tropospheric regions supporting deep

537   convection. The head-Bay of Bengal is known to be one of the regions where deep convection exists

538   prior to the onset of monsoon (Bhat et al., 2001). Since size distribution is a dominant factor in

539   determining the direct radiative forcing (Tegen and Lacis, 1996; Liao and Seinfeld, 1998; Seinfeld

540   et al., 2016), a clear seasonal change in the altitudinal variations of aerosol type and size distributions

541   associated with distinct transport and convective processes will have strong radiative impact.

542   Especially the columnar distribution of coarse mode dust and highly absorbing BC need explicit

543   representations in climate models for accurate understanding of the net TOA direct radiative forcing.

544   Apart from the direct radiative implications, abundance of coarse mode dust particles (having sizes

545   larger than critical diameter) and aged BC (coated with hygroscopic materials) in the lower free

546   troposphere can act as cloud condensation nuclei (CCN) in a supersaturated environment. Recent

547   studies suggest that mineral aerosols are the dominant ice nuclei for cirrus clouds (Storelvmo and

548   Herger, 2014).

549   **4. Summary and Conclusions**

550   Extensive air-borne measurements of aerosol number-size distribution profiles are carried out, for

551   the first time across the IGP prior to the onset of Indian summer monsoon. Collocated measurements

552   of BC profiles are also carried out. The main findings are:

553   • Aerosol size distribution depicted significant altitudinal variation in the coarse mode regime,

554   at western IGP (represented by JDR), having highest coarse mode mass fraction (72%) near

555   the surface; while BC mass fractions (F_{BC}) as well as aerosol accumulation and coarse mode

556   number concentrations (N_{AC}) remained nearly steady from surface to the ceiling altitude (~

557   3.5 km) of the aircraft measurements. However, the pattern was significantly different at

558   eastern IGP (represented by BBR) transforming to gradually decreasing values of M_C and

559   N_{AC}, but with a corresponding increase in the values of F_{BC} with altitude. At sub-regional

560   scales, BBR depicted higher spatial heterogeneity in the above aerosol characteristics; while

561   highest homogeneity was observed at JDR.

562   • Number concentrations showed dominance of accumulation mode near the surface, with the

563   Central IGP station Varanasi (VNS) depicting the highest values N_{AC} and (F_{BC} ~ 15%), while

564   the coarse mode remained nearly steady throughout the vertical column.

565   • Our measurements, supplemented with information from different space-borne sensors

566   (CATS aboard ISS; OMI) and model results clearly indicated role of mineral dust; both

567   locally generated and advected from the west Asian region, in contributing to the aerosol

568   loading across the IGP, especially at free-tropospheric altitudes. The vertical extents of these

569   layers reached as high as 5 km during the period of observation.

570 • Thermal power plants are important contributors to higher BC fraction at higher altitude over
571 the eastern part (BBR), while local anthropogenic sources are more prominent near the
572 surface at central IGP (VNS).

573

574 **Data availability**

575 Details of aircraft data used in this manuscript and the point of contact are available at
576 http://spl.gov.in; "Research Themes"; "Aerosols and Radiative Forcing".

577

578 **Authors contributions**

579 SSB, SKS and KKM conceptualized the experiment and finalized the methodology. SSB, MMG, VJ
580 and AV conducted the measurement on board aircraft. MMG carried out the scientific analysis of
581 the aircraft data and drafted the manuscript. KKM, SKS and SSB carried out the review and editing
582 of the manuscript.

583

584 **Competing interests**

585 The authors declare that they have no conflict of interest.

586

587 **Acknowledgement**

595

596

References

Ambient air quality status and trends in Odisha: 2006 – 2014: Published by State Pollution Control Board, Odisha, 2015.

Arnott, W. P., Hamasha, K., Moosmuller, H., Sheridan, P.J. and Ohren, J.A.: Towards aerosol light-absorption measurements with a 7-wavelength aethalometer: Evaluation with a photoacoustic instrument and 3-wavelength nephelometer. Aerosols Sci. Technol., 39(1), 17-29, 2005.

Babu, S.S., Nair, V.S., Gogoi, M.M. and Moorthy, K.K.: Seasonal variation of vertical distribution of aerosol single scattering albedo over Indian sub-continent: RAWEX aircraft observations. Atmos. Environ., 125, 312–323, https://doi.org/10.1016/ j.atmosenv.2015.09.041, 2016.

Banerjee, P., Satheesh, S.K., Moorthy, K.K., Nanjudiah, R.S., Nair, V.S.: Long-Range Transport of Mineral Dust to the Northeast Indian Ocean: Regional versus Remote Sources and the Implications, J. Climate, 32, 1525-1549, DOI: 10.1175/JCLI-D-18-0403.1, 2019.

Bansal, O., Singh, A., Singh, D.: Aerosol Characteristics over the Northwestern Indo-Gangetic Plain: Clear-Sky Radiative Forcing of Composite and Black Carbon Aerosol, Aerosol Air Quality Res., 19: 5–14, 2019.

Bhat, G.S., Gadgil, S., Kumar, P.V.S., Kalsi, S.R., Madhusoodanan, P., Murty, V.S.N., Rao, V.V.K.P., Babu, V.R., Rao, L.V.G., Rao, R.R., Ravichandran, R., Reddy, K.G., Rao, P.S., Sengupta, D., Sikka, D.R., Swain, J. and Vinayachandran, P.N.: BOBMEX: The Bay of Bengal Monsoon Experiment, Bull. American Met. Society. 82, 10, 2217-2243, 2001.

Bhattu, D., Tripathi, S., Chakraborty, A.: Deriving aerosol hygroscopic mixing state from size-resolved ccn activity and HR-TOF-AMS measurements, Atmos. Environ., 142, 57-70, 2016.

Brooks, J., James D.A., Paul I. et al.: Vertical and horizontal distribution of submicron aerosol chemical composition and physical characteristics across northern India during pre-monsoon and monsoon seasons. Atmos. Chem. Phys. 19, 5615–5634, 2019.

Corrigan, C.E., Ramanathan, V. and Schauer, J.J.: Impact of monsoon transitions on the physical and optical properties of aerosols. J. Geophys. Res., 111, D18208, doi:10.1029/2005JD006370, 2006.

Gautam, R., Hsu, N.C. and Lau, K.M.: Premonsoon aerosol characterization and radiative effects over theIndo-Gangetic Plains: Implications for regional climate warming, J. Geophys. Res., 115, D17208, doi:10.1029/2010JD013819, 2010.

Gautam, R., Hsu, N.C., Tsay, S.C., Lau, K.M., Holben, B., Bell, S. et al.: Accumulation of aerosols over the Indo-Gangetic plains and southern slopes of the Himalayas: distribution, properties

629   and radiative effects during the 2009 pre-monsoon season. Atmos. Chem. Phys. 11, 12841–
630   12863, 2011.

631   Giles, D. M., Holben, B. N., Eck, T. F., Sinyuk, A., Smirnov, A., Slutsker, I., Dickerson, R. R.,
632   Thompson, A. M. and Schafer, J. S.: An analysis of AERONET aerosol absorption properties
633   and classifications representative of aerosol source regions, J. Geophys. Res., 117, D17203,
634   doi:10.1029/2012JD018127, 2012.

635   Gogoi, M.M., Babu, S.S., Moorthy, K.K., Bhuyan, P.K., Pathak, B., Subba, T., Chutia, L., Kundu,
636   S.S., Bharali, C., Borgohain, A., Guha, A., De, B.K., Singh, B., and Chin, M.: Radiative effects
637   of absorbing aerosols over northeastern India: Observations and model simulations. J.
638   Geophys. Res., 122, doi:10.1002/2016JD025592, 2017.

639   Gogoi, M.M., Lakshmi, N.B., Nair, V.S., Kompalli, S.K., Moorthy, K.K. and Babu, S.S., 2019.
640   Seasonal contrast in the vertical profiles of aerosol number concentrations and size
641   distributions over India: implications from RAWEX aircraft campaign. J. Earth Sys. Sc., 128
642   225, DOI: 10.1007/s12040-019-1246-y, 2019.

643   Govardhan, G., Satheesh, S.K., Moorthy, K.K. and Nanjundiah, R.: Simulations of Black Carbon
644   Over Indian Region: Improvements and implications of diurnality in emissions Atmos. Chem.
645   Phys. Discuss., https://doi.org/10.5194/acp-2019-152, 2019.

646   Jayachandran, V.N., Babu, S.S., Vaishya, V., Gogoi, M.M., Nair, V.S., Satheesh, S.K., Moorthy,
647   K.K.: Altitude profiles of cloud condensation nuclei characteristics across the Indo-Gangetic
648   Plain prior to the onset of the Indian summer monsoon, Atmos. Chem. Phys., 20, 561–576,
649   2020, doi:10.5194/acp-20-561-2020, 2020

650   Kedia, S., Ramachandran, S., Holben, B.N., Tripathi, S.N.: Quantification of aerosol type, and
651   sources of aerosols over the Indo-Gangetic Plain. Atmos. Env., 98, 607-619, 2014.

652   Kirchstetter, T. W., Novakov, T. and Hobbs, P. V.: Evidence that the spectral dependence of light
653   absorption byaerosols is affected by organic carbon,J. Geophys. Res.,109, D21208,
654   doi:10.1029/2004JD004999, 2004.

655   Konwar, M., Panicker, A.S., Axisa, D. and Prabha, T.V.: Near cloud aerosols in monsoon
656   environment and its impact on radiative forcing. J. Geophys. Res., doi: 10.1002/
657   2014JD022420, 2015.

658   Kumar, M., Parmar, K.S., Kumar, D.B., Mhawish, A., Broday, D.M., Malla, R.K., Banerjeea, T.:
659   Long-term aerosol climatology over Indo-Gangetic Plain: Trend, prediction and potential
660   source fields. Atmos. Env., 180, 37–50, 2018.

661 Lee et al.: Investigation of CATS aerosol products and application toward global diurnal variation
662   of aerosols, Atmos. Chem. Phys. Discuss., https://doi.org/10.5194/acp-2018-1298 2019.

663 Levelt, P. F., van den Oord, G. H. J., Dobber, M. R., Mälkki, A., Visser, H., de Vries, J., Stammes,
664   P., Lundell, J. O. V., and Saari, H.: The Ozone Monitoring Instrument, IEEE Trans. Geosci.
665   Remote Sens., 44, 1093–1101, doi:10.1109/TGRS.2006.872333, 2006.

666 Li, Z., et al.:Aerosol and monsoon climate interactions over Asia, Aerosol and monsoon climate
667   interactions over Asia, Rev. Geophys., 54, 866–929, doi:10.1002/2015RG000500, 2016.

668 Liao, H. and Seinfeld, J.H.: Radiative forcing by mineral dust aerosols: Sensitivity to key variables.
669   J. Geophys. Res., 103, 31,637–31, 645, 1998.

670 Mhawish, A., Banerjeea, T., Broday, D.M., Misra, A., Tripathi, S.N.: Evaluation of MODIS
671   Collection 6 aerosol retrieval algorithms over IndoGangetic Plain: Implications of aerosols
672   types and mass loading, Remote Sens. Env., 201, 297–313, 2017.

673 Miller, R. L. et al.: Mineral dust aerosols in the NASA Goddard Institute for Space Sciences ModelE
674   atmospheric general circulation model. J. Geophys. Res. 111, D06208,
675   doi:10.1029/2005JD005796, 2006.

676 Mitchell, J.P. and Nagel, M.W., Time-of-flight aerodynamic particle size analysers: their use and
677   limitations for the evaluation of medical aerosols, J. Aerosol. Medicine, 12, 4, 217-240,
678   1999.

679 Moorthy, K. K., Babu, S.S., Satheesh, S.K., Srinivasan, J. and Dutt, C.B.S.: Dust absorption over
680   the ''Great Indian Desert'' inferred using ground-based and satellite remote sensing, J.
681   Geophys. Res., 112, D09206, doi:10.1029/2006JD007690, 2007.

682 Moorthy, K.K., Babu, S.S., Satheesh, S.K., Srinivasan, J. and Dutt, C.B.S.: Dust absorption over the
683   ''Great Indian Desert'' inferred using ground-based and satellite remote sensing. J. Geophys.
684   Res., 112, D09206, doi:10.1029/2006JD007690, 2007.

685 Moorthy, K.K., Satheesh, S.K. and Kotamarthi, V.R., Evolution of aerosol research in India and
686   the RAWEX–GVAX: an overview, Current Sc., 111, 1, 2016.

687 Moorthy, K.K., Satheesh, S.K., Murthy, B.V.K.: Characteristics of spectral optical depths and size
688   distributions of aerosols over tropical oceanic regions, J. Atmos. Sol. Terr. Phys., 60, 981-992,
689   1998.

690 Nair, V. S., Babu, S.S., Gogoi, M.M. and Moorthy, K.K.: Large-scale enhancement in aerosol
691   absorption in the lower free troposphere over continental India during spring, Geophys. Res.
692   Lett., 43, 11,453–11,461, doi:10.1002/2016GL070669, 2016.

693 Nath, R., Luo, Y., Chen, W. and Cui, X.: On the contribution of internal variability and external
694   forcing factors to the Cooling trend over the Humid Subtropical Indo-Gangetic Plain in India.
695   Sci. Reports., 8:18047, DOI:10.1038/s41598-018-36311-5, 2018.

696 Padmakumari, B., Maheskumar, R.S., Harikishan, G., Morwal, S.B., Prabha, T.V., Kulkarni, J.R.:
697   In situ measurements of aerosol vertical and spatial distributions over continental India during
698   the major drought year 2009, Atmos. Env., 80, 107-121, 2013.

699 Panda, U., Das, T.: Micro-structural analysis of individual aerosol coarse particles during different
700   seasons at an eastern coastal site in India. Atmos. Pollution Res., DOI:
701   10.1016/j.apr.2016.08.012, 2016.

702 Pandey, S.K., Vinoj, V., Landu, K. and Babu, S.S.: Declining pre-monsoon dust loading over South
703   Asia: Signature of a changing regional climate. Sci. Reports., 7:16062, DOI:10.1038/s41598-
704   017-16338-w, 2017.

705 Pillai, P. S., and Moorthy, K.K.: Aerosol mass-size distributions at a tropical coastal environment:
706   Response to mesoscale and synoptic processes, Atmos. Environ., 35, 4099– 4112, 2001.

707 Praveen, P.S., Ahmed, T., Kar, A., Rehman, I.H. and Ramanathan, V.: Link between local scale BC
708   emissions in the Indo-Gangetic Plains and large scale atmospheric solar absorption, Atmos.
709   Chem. Phys., 12, 1173–1187, 2012.

710 Rana, A., Jia, S., Sarkar, S.: Black carbon aerosol in India: A comprehensive review of current status
711   and future prospects. Atmos. Res., 218, 207–230, 2019.

712 Seinfeld, J.H. et al., 2016. Improving our fundamental understanding of the role of aerosol-cloud
713   interactions in the climate system. Proc. Natl. Acad. Sci. U S A. 113(21): 5781–5790.

714 Singh, A., Khadak S.M., Ruphaketi, M., Junkermann, W., Panday, A.K., Lawrence, M.G.: An
715   overview on the airborne measurement in Nepal, part 1: vertical profile of aerosol size-number,
716   spectral   absorption   and   meteorology.   Atmos.   Chem.   Phys.   Discuss.
717   https://doi.org/10.5194/acp-2018-95, 2018.

718 Srivastava, R.: Trends in aerosol optical properties over South Asia, Int. J. Climatol., 37, 1, 371-
719   380, DOI: 10.1002/joc.4710, 2016.

720 Storelvmo, T. and Herger, N.: Cirrus cloud susceptibility to the injection of ice nuclei in the upper
721   troposphere. J. Geophys. Res. 119, doi:10.1002/2013JD020816, 2014.

722 Tegen, I. and Lacis, A. A.: Modelling of particle size distribution and its influence on the radiative
723   properties of mineral dust aerosol, J. Geophys. Res.,101, 19,237–19,244 1996.

724   Vadrevu, K.P., Ellicott, E., Badarinath, K.V.S., Vermote, E.: MODIS derived fire characteristics and
725   aerosol optical depth variations during the agricultural residue burning season, north India,
726   Env. Pollution, 159, 1560-1569, 2011.

727   Vaishya, A., Babu, S.S., Jayachandran, V., Gogoi, M.M., Lakshmi, N.B., Moorthy, K.K. and
728   Satheesh, S.K.: Large contrast in the vertical distribution of aerosol optical properties and
729   radiative effects across the Indo-Gangetic Plain during the SWAAMI–RAWEX campaign.
730   Atmos. Chem. Phys., 18, 17669–17685, 2018.

731   Venkataraman, C., Habib, G., Kadamba, D., Shrivastava, M., Leon, J.F., Crouzille, B., Boucher, O.
732   and Streets, D.G.: Emissions from open biomass burning in India: Integrating the inventory
733   approach with high-resolution Moderate Resolution Imaging Spectroradiometer (MODIS)
734   active-fire and land cover data, Global Biogeochem. Cycles, 20, GB2013,
735   doi:10.1029/2005GB002547, 2006.

736   Weingartner, E., Saathoff, H., Schnaiter, M., Streit, N., Bitnar, B. and Baltensperger, U.: Absorption
737   of light by soot particles: Determination of the absorption coefficient by means of
738   aethalometers. J. Aerosol Sci. 34, 1445– 1463, 2003.

739   Yorks, J. E.: An overview of the CATS level 1 processing algorithms and data products, Geophys.
740   Res. Lett., 43, 4632–4639, doi:10.1002/2016GL068006, 2016.

741   Yorks, J. E.: The Airborne Cloud–Aerosol Transport System: Overview and Description of the
742   Instrument and Retrieval Algorithms, J. Atmos. Oceanic Tech., 31, 2482-2497, doi:
743   10.1175/JTECH-D-14-00044.1, 2014.

744

745   *****